

RESEARCH

Open Access



Postnatal meningeal CSF transport is primarily mediated by the arachnoid and pia maters and is not altered after intraventricular hemorrhage-posthemorrhagic hydrocephalus

Shelei Pan¹, Joshua P. Koleske¹, Gretchen M. Koller¹, Grace L. Halupnik¹, Abdul-Haq O. Alli¹, Shriya Koneru¹, Dakota DeFreitas¹, Sruthi Ramagiri¹ and Jennifer M. Strahle^{1*}

Abstract

Background CSF has long been accepted to circulate throughout the subarachnoid space, which lies between the arachnoid and pia maters of the meninges. How the CSF interacts with the cellular components of the developing postnatal meninges including the dura, arachnoid, and pia of both the meninges at the surface of the brain and the intracranial meninges, prior to its eventual efflux from the cranium and spine, is less understood. Here, we characterize small and large CSF solute distribution patterns along the intracranial and surface meninges in neonatal rodents and compare our findings to meningeal CSF solute distribution in a rodent model of intraventricular hemorrhage-posthemorrhagic hydrocephalus. We also examine CSF solute interactions with the tela choroidea and its pial invaginations into the choroid plexuses of the lateral, third, and fourth ventricles.

Methods 1.9-nm gold nanoparticles, 15-nm gold nanoparticles, or 3 kDa Red Dextran Tetramethylrhodamine constituted in aCSF were infused into the right lateral ventricle of P7 rats to track CSF circulation. 10 min post-1.9-nm gold nanoparticle and Red Dextran Tetramethylrhodamine injection and 4 h post-15-nm gold nanoparticle injection, animals were sacrificed and brains harvested for histologic analysis to identify CSF tracer localization in the cranial and spine meninges and choroid plexus. Spinal dura and leptomeninges (arachnoid and pia) wholemounts were also evaluated.

Results There was significantly less CSF tracer distribution in the dura compared to the arachnoid and pia maters in neonatal rodents. Both small and large CSF tracers were transported intracranially to the arachnoid and pia mater of the perimesencephalic cisterns and tela choroidea, but not the falx cerebri. CSF tracers followed a similar distribution pattern in the spinal meninges. In the choroid plexus, there was large CSF tracer distribution in the apical surface of epithelial cells, and small CSF tracer along the basolateral surface. There were no significant differences in tracer intensity in the intracranial meninges of control vs. intraventricular hemorrhage-posthemorrhagic hydrocephalus (PHH) rodents, indicating preserved meningeal transport in the setting of PHH.

Conclusions Differential CSF tracer handling by the meninges suggests that there are distinct roles for CSF handling between the arachnoid-pia and dura maters in the developing brain. Similarly, differences in apical vs. luminal choroid plexus CSF handling may provide insight into particle-size dependent CSF transport at the CSF-choroid plexus border.

*Correspondence:

Jennifer M. Strahle
strahlej@wustl.edu

Full list of author information is available at the end of the article



© The Author(s) 2024. **Open Access** This article is licensed under a Creative Commons Attribution 4.0 International License, which permits use, sharing, adaptation, distribution and reproduction in any medium or format, as long as you give appropriate credit to the original author(s) and the source, provide a link to the Creative Commons licence, and indicate if changes were made. The images or other third party material in this article are included in the article's Creative Commons licence, unless indicated otherwise in a credit line to the material. If material is not included in the article's Creative Commons licence and your intended use is not permitted by statutory regulation or exceeds the permitted use, you will need to obtain permission directly from the copyright holder. To view a copy of this licence, visit <http://creativecommons.org/licenses/by/4.0/>. The Creative Commons Public Domain Dedication waiver (<http://creativecommons.org/publicdomain/zero/1.0/>) applies to the data made available in this article, unless otherwise stated in a credit line to the data.

Introduction

The role of the meninges in CSF circulation has historically been a subject of longstanding speculation. Nineteenth century French physiologist Francois Magendie, who discovered the eponymous foramen of Magendie, postulated that the leptomeninges (pia and arachnoid mater) produce CSF [1, 2]. Even though this theory was later disregarded due to histologic, pharmacologic, and physiologic studies supporting the choroid plexus (ChP) as the site of CSF production [3–8], his discoveries highlighted that the meninges are more than a protective barrier. Our understanding of the structural and functional complexities of the meninges has expanded with more recent investigations elucidating specific roles the meninges actively take in the development, maintenance, and function of the CNS. In fetal development, the meninges play an important role in releasing diffusible factors which influence the proliferation and migration of brain parenchyma and epithelial cells [9]. In the adult rodent CNS, the meningeal lymphatics within the dorsal convexities and at the base of the skull play a role in CNS immune surveillance and CSF solute handling [10, 11] alongside other routes of CSF drainage including CSF efflux along the perivascular and perineural subarachnoid spaces (SAS) into the extracranial lymphatics of the skull base [12]. The leptomeninges and dura mater have different transcriptional signatures and play distinct roles within the CNS [13]. Beyond their spatial heterogeneity, meningeal fibroblasts also have distinct transcriptional signatures across development [13], however it is not clear if meningeal CSF solute handling during development differs from what is observed in adult and aged animals. Additionally, it is not clear if there are differences in CSF handling within the layers of the neonatal meninges including the arachnoid and pia (vs. dura). As there is a complex relationship between the meninges and CSF, it is important to understand how and where in the postnatal meninges CSF is handled.

Particularly relevant to the neonatal and postnatal time period, understanding how the developing meninges handle CSF may also have implications for neurological sequelae after devastating pathologies like neonatal intraventricular hemorrhage-posthemorrhagic hydrocephalus (IVH-PHH). IVH in neonates most commonly occurs as a result of bleeding from the germinal matrix and can cause brain injury and PHH [14]. While PHH has previously been hypothesized to alter intraventricular CSF dynamics, it is unknown how IVH-PHH affects meningeal CSF handling. As many intracranial cisterns are lined by the leptomeninges and adjacent neurodevelopmentally vital structures like the hippocampus and brainstem, understanding postnatal meningeal CSF handling may help provide insight into how neurotoxic blood

breakdown products released into the CSF spaces after IVH-PHH may be transported beyond the ventricular system to the developing brain.

In the present study, we present a CNS-wide characterization of CSF solute movement within the meninges and its related structures in neonatal rodents, with special emphasis on the intracranial meninges, spinal meninges, and ChP. Using intraventricular injections of large (15-nm) and small (1.9-nm and 3 kDa) CSF tracers, we show that both large and small CSF tracers distribute primarily within the cranial and spine leptomeninges with more limited distribution within the dura. Both large and small CSF tracers circulate through the leptomeninges of the perimesencephalic cisterns and are also present in the third ventricular tela choroidea and velum interpositum, a distribution pattern that is not affected by IVH-PHH. In the ChP, small CSF tracers are found in the basolateral surface of the ChP epithelial cells, while large CSF tracers preferentially accumulate on the apical surface. Finally, meningeal transport is preserved early after PHH and may act as a route to transmit both physiologic CSF solutes and blood breakdown products after IVH.

Methods

Animals (Rodents)

All experiments were approved by the Institutional Animal Care and Use Committee of Washington University (protocol #22-0614). Sprague Dawley Rats (crl:SD400, Charles River Laboratories, Wilmington, MA) were used in all experiments. Female and male post-natal day 4–7 Sprague Dawley Rats were housed with their dams in a 12-h light–dark cycle in a temperature and humidity-controlled room. Water and food were provided ad libitum for the dam.

Intraventricular hemorrhage-posthemorrhagic hydrocephalus induction

P4 rodents were anesthetized (isoflurane 2–3% induction and 1.5% maintenance) and fixed in a stereotaxic frame. A 2.5 mm midline incision was made and a 0.3 cc syringe with a 30-gauge needle was inserted into the right lateral ventricle (LV) at the following coordinates from bregma: 1.4 mm lateral, 0.5 mm anterior, and 2.0 mm deep. A small volume (20 μ L) of artificial CSF (aCSF) (Tocris Bioscience, Bristol, UK) or hemoglobin constituted in aCSF at a 150 mg/mL concentration was injected at a rate of 8000 nL/min using a micro-infusion pump (World Precision Instruments, Sarasota, FL) to create the aCSF control and IVH-PHH conditions respectively. The needle was left in for 5 min post injection to prevent backflow. The incision was closed with 6–0 Ethilon suture (Ethicon Inc, Raritan, NJ). Rodents recovered from anesthesia and were returned to their cage with the dam for 72 h before

CSF tracer injection at P7. Rats injected with hemoglobin developed ventriculomegaly by the time of tracer injection at P7 [15–17].

CSF tracer injections

Anesthetized naïve (Figs. 1B–D, 2B, 4B–D, 5B, 8), aCSF control (Figs. 1F, 2C–G, 3, 4E, 5C–J, 6, 7), and IVH-PHH (Figs. 2H–J, 5K–M) P7 rats underwent intraventricular injection of 20 µl of 3 kDa Red Dextran Tetramethylrhodamine (RD/TMR) (D3307, Thermo Fisher Scientific, Waltham, MA), 1.9-nm (1102, Nanoprobes, Yaphank, NY), or 15-nm (1115, Nanoprobes,

Yaphank, NY) gold nanoparticles (AuNPs) as per the protocol above with the following coordinates from bregma: 1.7 mm lateral, 0.5 mm anterior, and 2.0 mm deep. 1.9- and 15-nm AuNPs were constituted in aCSF at a concentration of 200 mg/mL, while RD/TMR was dissolved in aCSF in a 0.25% w/v solution. Rodents were deeply anesthetized with isoflurane and sacrificed with intracardial perfusion with 10 mL of ice-cold PBS followed by 10 mL of 4% PFA at 10 min after 1.9-nm AuNP and 3 kDa RD/TMR injections or 4 h after 15-nm AuNP injections.

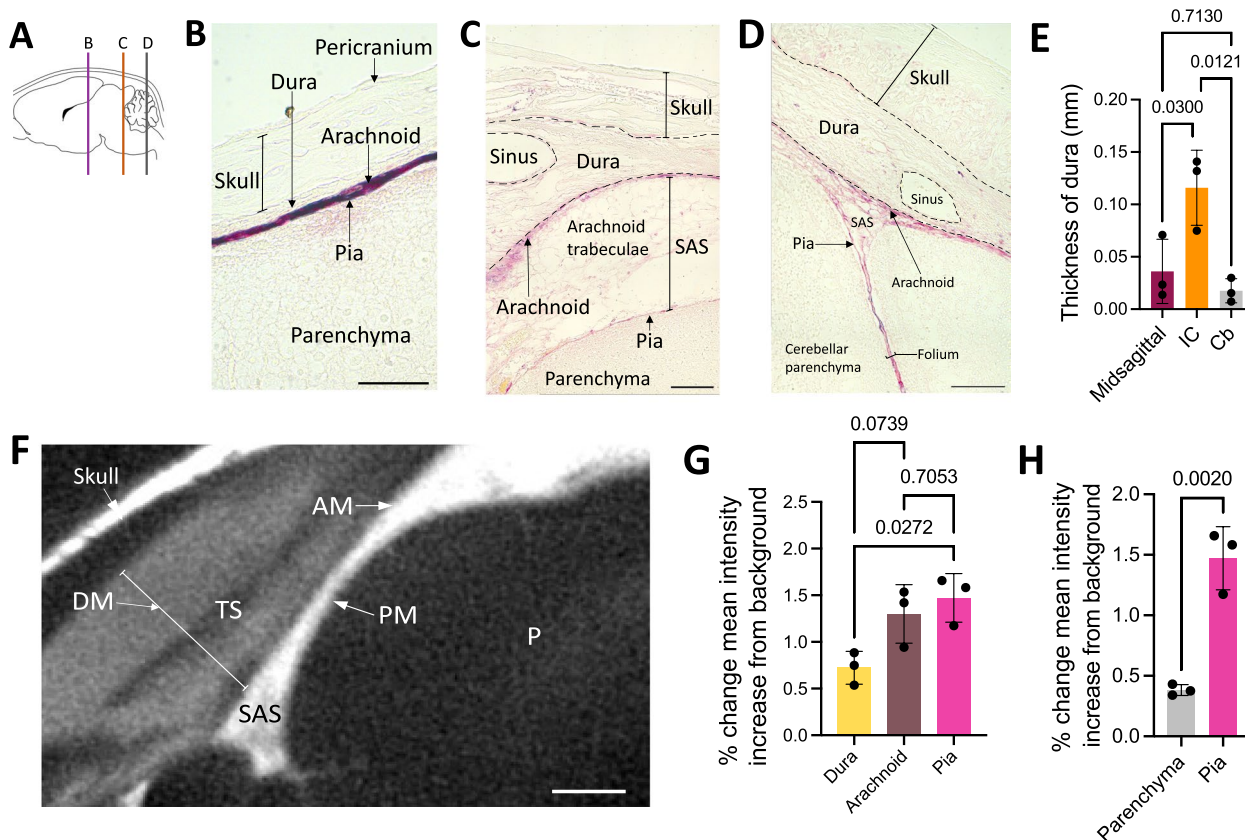


Fig. 1 Large CSF tracers primarily circulate within the neonatal arachnoid and pia maters and not the dura. **A** Schematic of regions shown in **B–D**. **B–D**, Representative histology of decalcified skulls and the underlying meninges and parenchyma over the cortex (**B**), inferior colliculus (**C**), and cerebellum (**D**) showing minimal large CSF tracer (magenta) distribution through the pericranium, skull, and dura mater, but widespread distribution within the arachnoid and pia maters 4 h after 15-nm gold nanoparticle (AuNP) injection into the right lateral ventricle of P7 rats. There was also limited AuNP influx into the parenchyma. The subarachnoid space (SAS) is collapsed post-mortem and differentiation between layers was primarily based on tissue morphology. scalebars = 50 µm. **E** Quantification of the thickness of the midsagittal dura over the longitudinal fissure, the inferior colliculus (IC), and cerebellum (Cb). Data are mean ± SD, n = 3 per group; One-way ANOVA with post-hoc Tukey. **F** Representative X-ray microtomography (XRM) image showing high amounts of AuNP enhancement within the arachnoid mater (AM), pia mater (PM), and SAS, with less enhancement in the dura mater (DM). There was minimal enhancement in the lumen of the transverse sinus (TS) and parenchyma (P). scalebar = 500 µm. **G, H** Quantification of the percent change in mean intensity increase of 15-nm AuNPs in the dura, arachnoid, and pia maters (**G**) and the pia mater and parenchyma (**H**) compared to the background XRM signal. Data are mean ± SD, n = 3 per group; **G** One-way ANOVA with post-hoc Tukey. **H** Unpaired, two-tailed t-test All data are representative of 3 rodents

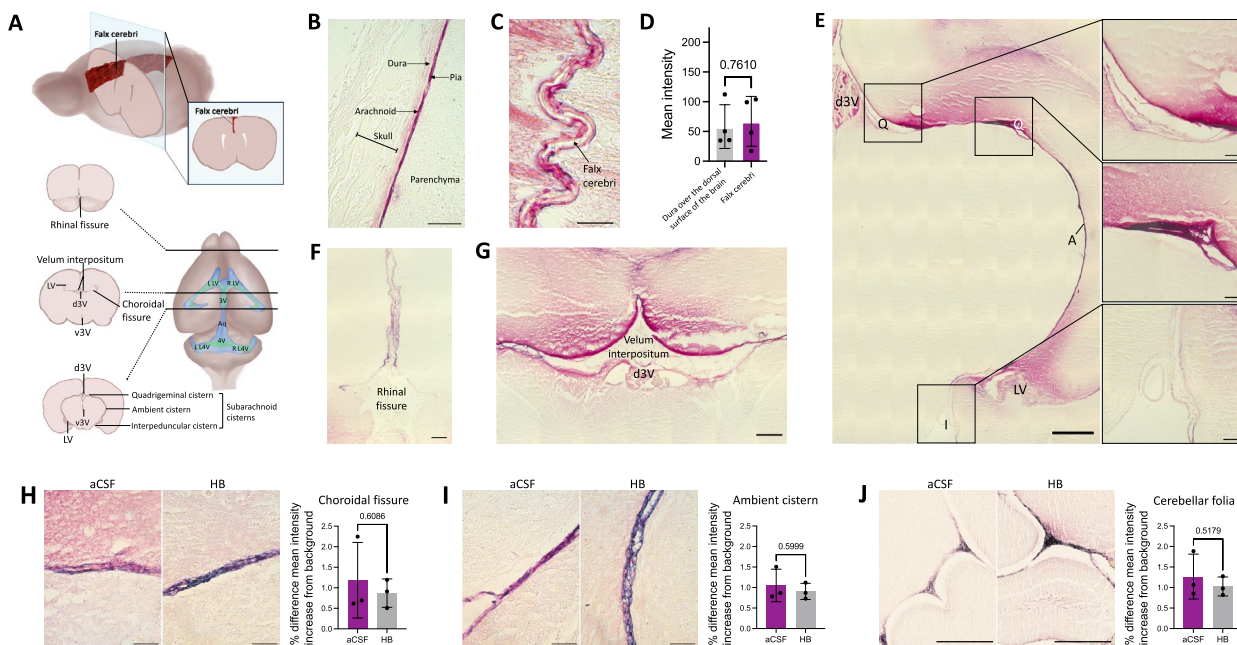


Fig. 2 Distribution of large CSF tracers within the intracranial meninges. **A** Schematic showing location of meningeal, cerebral ventricular, and choroid plexus structures highlighted in **B–I**. **B** Representative histology of the meninges at the dorsal surface of the brain (including the dura, arachnoid, and pia maters) and the overlying decalcified skull 4 h after 15-nm gold nanoparticle (AuNP) injection into the right lateral ventricle of P7 rats. scalebar = 50 μ m. **C** Representative histology showing 15-nm AuNP distribution within the falx cerebri and leptomeningeal (pia and arachnoid) invaginations into the longitudinal fissure. The falx cerebri is labeled with a black arrow. scalebar = 25 μ m. **D** Quantification of the mean intensity of 15-nm AuNP distribution within the dura mater over the surface of the brain compared to the falx cerebri. Data are mean \pm SD, $n = 3$ per group; Unpaired, two-tailed t-test. **E** Representative histology showing 15-nm AuNP circulation through the dorsal third ventricle (d3V), quadrigeminal cistern (Q), ambient cistern (A), interpeduncular cistern (I), and lateral ventricle (LV) 4 h after intraventricular injection in P7 rodents. E scalebar = 500 μ m, E inset scalebars = 75 μ m. **F, G** 15-nm AuNP distribution in the rhinal fissure (**F**) and velum interpositum (**G**). VI: velum interpositum; d3V: dorsal third ventricle. F scalebar = 100 μ m, G scalebar = 250 μ m. **H–J** 15-nm AuNP distribution in the choroidal fissure (**H**), ambient cistern (**I**), and cerebellar folia (**J**) 4 h post-15-nm AuNP injection into the right lateral ventricle of rats with intraventricular hemorrhage-posthemorrhagic hydrocephalus (IVH-PHH, induced 72 h before AuNP injection with intraventricular hemoglobin (HB)) and aCSF control rats. **H, I** scalebars = 50 μ m, **J** scalebars = 250 μ m. Quantifications are also shown as mean \pm SD with unpaired two-tailed t tests, $n = 3$ animals per group. All data are representative of 3 rodents

Sample preparation for meninges analysis using light microscopy

After intracardial perfusion and sacrifice, the cranium was harvested whole in a subset of rodents (Figs. 1B–D, 2B, H–J 4B–D, 5B, K–M, 8). Micro scissors were used to remove soft tissue down to the bone, before the cranium was left in 4% PFA overnight for fixation. After fixation, the cranium was rinsed in running water for 1 h and placed in 8% hydrochloric acid (HCl) or 0.12 M EDTA in PBS for 24–48 h for decalcification. After decalcification, the cranium was rinsed in running water for 2 h. Rodents that did not undergo decalcification of the cranium/spine (Figs. 2C–G, 3, 4E, 5C–J, 6, 7) had their brain/spinal cord harvested immediately after perfusion and were placed in 4% PFA overnight for fixation.

After decalcification/fixation, the cranium and/or brain was washed 2 \times in PBS for 1 h each, then immersed in 30% and 50% ethanol for 30 min each, before being transferred to 70% ethanol for 24 to 72 h at 4 $^{\circ}$ C prior to

xylene and paraffin processing. The cranium/brain was embedded in paraffin, and 8–12 μ m thick slices were sectioned in the coronal planes using a microtome. For sections of the tela choroidea shown in Fig. 5, sections were obtained at a 15 degree angle from coronal to show the course of the tela choroidea from the roof of the third ventricle (3V) to the LV. Slides were incubated overnight at 60 $^{\circ}$ C before sections were soaked in xylene for 20 min and mounted with Permount mounting medium (#SP15-100, Thermo Fisher Scientific, Waltham, MA) for light microscopy localization of AuNPs, or proceeding with immunohistochemistry for immunostaining and fluorescent microscopy co-localization of RD/TMR with meningeal fibroblast markers.

Immunohistochemistry of RD/TMR crania

After xylene, sections were rehydrated with immersion in 100%, 95%, 70%, 50%, and 30% ethanol for 5 min each. After 5 min in deionized H₂O, heat-mediated

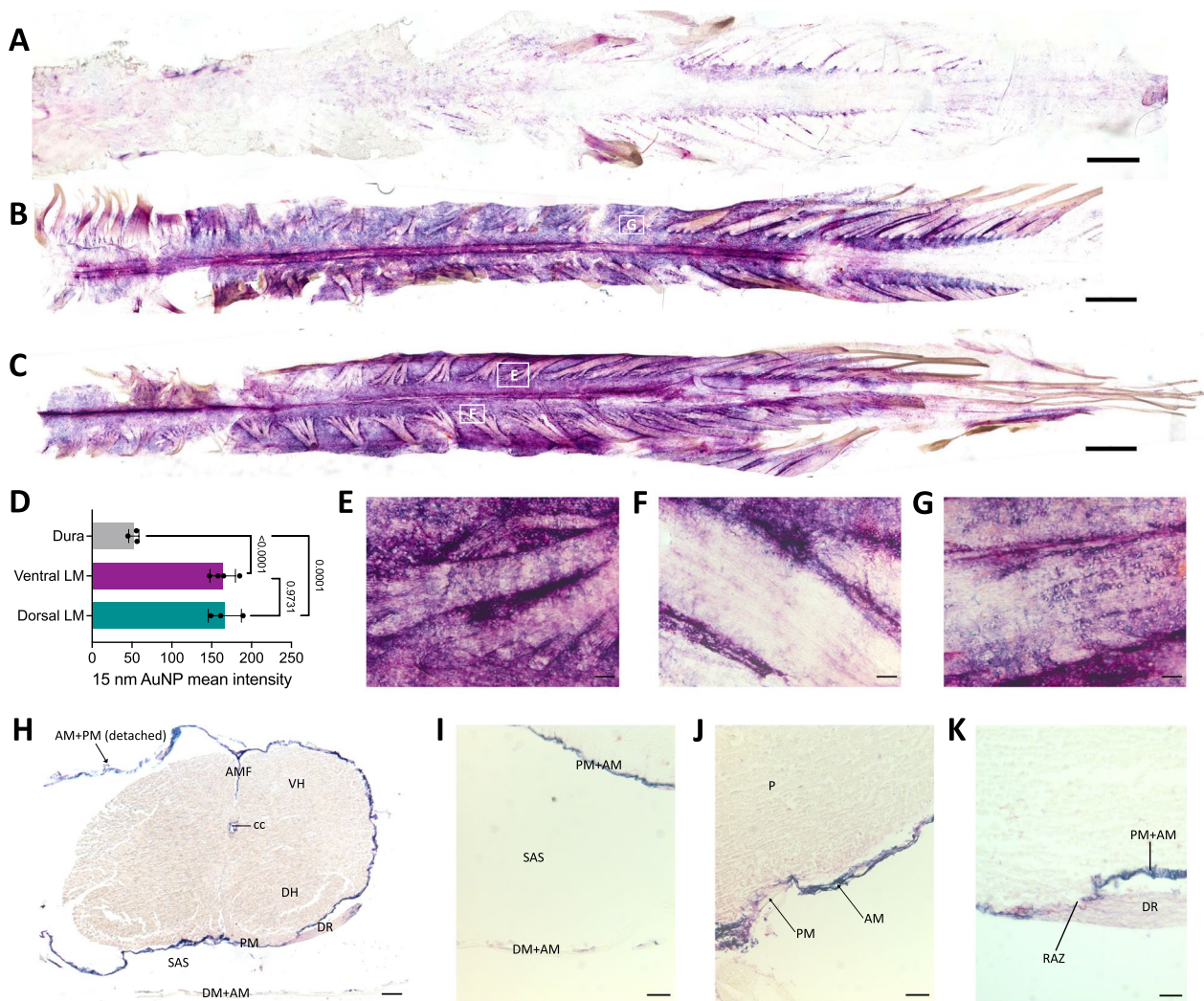


Fig. 3 Large CSF tracers preferentially circulate within the spinal leptomeninges with limited entry superiorly into the spinal dura and inferiorly into the underlying parenchyma. **A, B** Representative wholemounts showing large CSF tracer distribution through the dorsal spinal cord dura (**A**) and dorsal spinal cord leptomeninges (pia and arachnoid) (**B**) 4 h after 15-nm gold nanoparticle (AuNP) injection into the right lateral ventricle of P7 rodents. Scalebar = 1 cm. **C** Representative wholemount showing 15-nm AuNP distribution through the ventral spinal cord leptomeninges 4 h after intraventricular injection into the right lateral ventricle of P7 rodents. Scalebar = 1 cm. **D**, Quantification of 15-nm AuNP mean intensity in the spine dura, ventral leptomeninges, and dorsal leptomeninges. There was significantly more 15-nm AuNP distribution in the leptomeninges than the dura. Data are mean \pm SD, $n = 3$ per group; One-way ANOVA with post-hoc Tukey. **E–G** High magnification histology of 15-nm AuNP distribution along the leptomeninges of spinal nerve roots as they leave the spinal cord. 15-nm AuNPs distributed primarily around the roots (**F**), with additional diffuse 15-nm AuNPs observed inside the roots (**E, G**). Areas from which high-magnification images are obtained are indicated by white boxes in 2B and 2C. **E–G** scalebars = 25 μ m. **H–K** Representative histology showing 15-nm AuNP distribution in the spinal cord, spinal leptomeninges and spinal dura mater. The anterior median fissure (AMF), central canal (cc), dorsal horn (DH), dorsal root (DR), dura mater (DM), arachnoid mater (AM), pia mater (PM), ventral horn (VH), subarachnoid space (SAS), root attachment zone (RAZ), and parenchyma (P) are indicated. **H** scalebar = 1 mm, **I–K** scalebars = 25 μ m. All data are representative of 3 rodents

antigen retrieval was performed with 10 \times Diva DeCloaker (DV2004MX, BioCare Medical, Pacheco CA). Slides were cooled to room temperature before being rinsed with 1 \times PBS 6 times for 5 min each and blocked in goat serum (5% normal goat serum, 2.5% BSA, 0.5% TX-100) (S-1000-200, Vector Laboratories, Newark, CA) for 1 h. Sections were incubated

overnight at 4 $^{\circ}$ C in the following primary antibodies diluted in TBST: 1:200 dilution of anti-CRABP2 (MAB5488, EMD Millipore/Sigma Aldrich, St. Louis MO), 1:200 dilution of anti-RALDH2 (#13951-1-AP, Proteintech/Sigma Aldrich, St. Louis MO), 1:100 dilution of anti-ZO-1 (ab96587, Abcam, Cambridge MA). After incubation, sections were rinsed in PBS 6 times

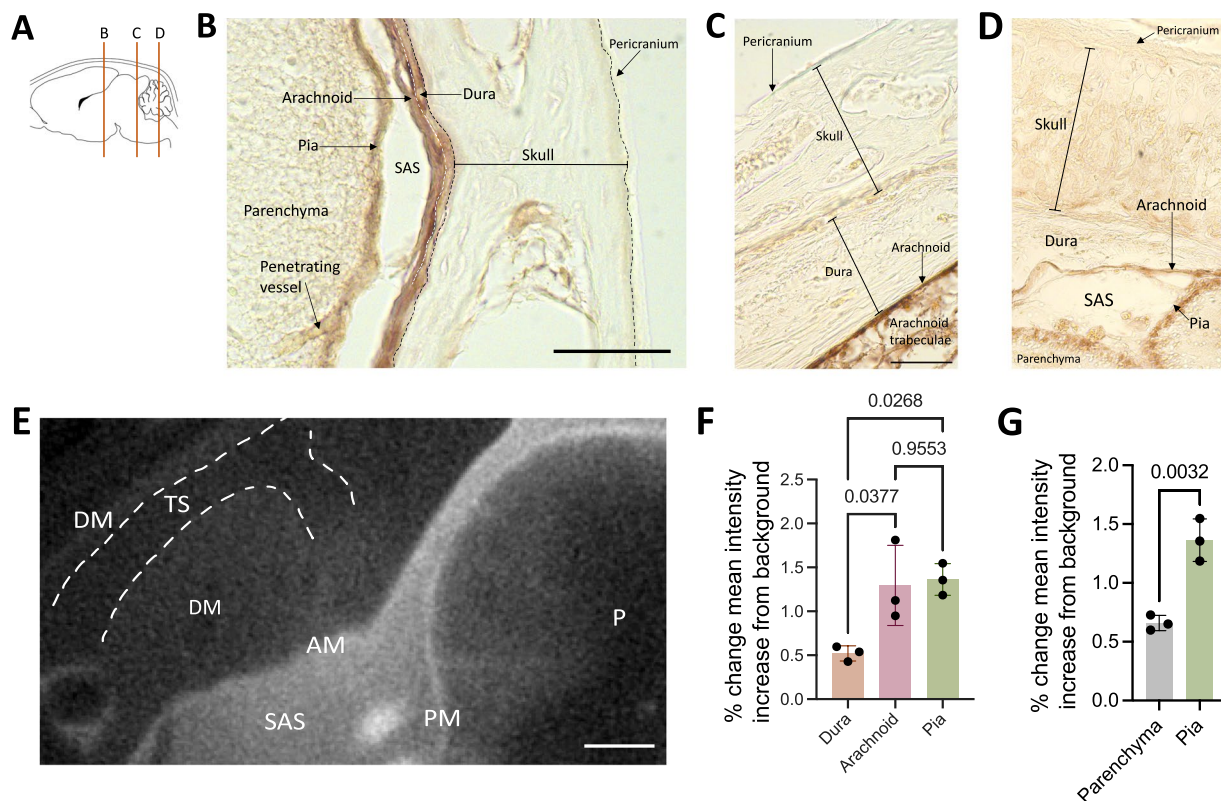


Fig. 4 Small CSF tracers primarily circulate within the leptomeninges and not the dura. **A** Schematic of regions shown in **B–D**. **B–D** Representative histology of decalcified skulls and the underlying meninges and parenchyma showing widespread small CSF tracer distribution within the arachnoid and pia maters over the cortex (**B**), inferior colliculus (**C**), and cerebellum (**D**) 10 min after 1.9-nm gold nanoparticle (AuNP) injection into the right lateral ventricle of P7 rats. There was minimal 1.9-nm AuNP (brown) distribution through the pericranium and skull, and limited tracer distribution through the dura mater along the surface of the brain. The subarachnoid space is collapsed post-mortem and differentiation between layers was primarily based on tissue morphology. scalebar = 50 μ m. **E** Representative X-ray microtomograph (XRM) showing 1.9-nm AuNP distribution within the pia mater (PM), arachnoid mater (AM), subarachnoid space (SAS), and parenchyma (P) at the level of the inferior colliculus. Similar to observations on histology, there was minimal enhancement in the dura mater (DM) and little to no enhancement in the transverse sinus (TS, dashed white line). scalebar = 500 μ m. **F, G** Quantification of the percent change in mean intensity increase of 1.9-nm AuNPs in the dura, arachnoid, and pia maters (**F**) and pia mater and parenchyma (**G**) compared to the background XRM signal. Data are mean \pm SD, $n=3$ per group; **F** One-way ANOVA with post-hoc Tukey. **G** Unpaired, two-tailed T test. All data are representative of 3 rodents

for 5 min each followed by incubation for 60 min at room temperature with the appropriate secondary antibodies diluted in TBST: 1:2000 dilution of goat anti-mouse IgG Alexa Fluor 488 (#A-32723, Thermo Fisher Scientific, Waltham MA), 1:2000 dilution of goat anti-rabbit IgG Alexa Fluor 647 (#A-21244, Thermo Fisher Scientific, Waltham MA). Secondary antibodies were washed off with PBS 5–6 times for 5 min each before incubation with a 1:500 dilution (in PBS) of 5 mg/mL DAPI for 5 min in the dark at room temperature. Sections were washed with PBS 3–5 times for 5 min each and mounted with ProLong Gold Antifade Mountant (#P36930, Thermo Fisher Scientific, Waltham MA). Confocal images were taken with the 20 \times and 40 \times (oil) lenses on a Zeiss LSM 880 Airyscan inverted two-photon microscope (Carl Zeiss Imaging, White Plains, NY).

AuNP quantifications from light microscope images

15-nm AuNPs appear magenta on gross visualization/light microscopy, while 1.9-nm AuNPs appear brown. Quantifications in Figs. 2D, 3D, 5D, and 7 were obtained by first opening photomicrographs in Fiji (version 2.3.0/1.53q). Images were converted to an 8-bit image type before inverting the color. Five random areas per image were analyzed for mean intensity and averaged. For quantification of the ChP (Fig. 7), the apical and basolateral surfaces of the ChP epithelial cells were identified by morphology. Averaged values were compared with statistical analyses; for comparisons with 2 groups (7B–D, 7H–J), unpaired, two-tailed t tests were performed. For comparisons with 3 groups (7E–F, 7K–L), one-way ANOVAs with post-hoc Tukeys were performed. Quantifications of dural thickness in Fig. 1E were

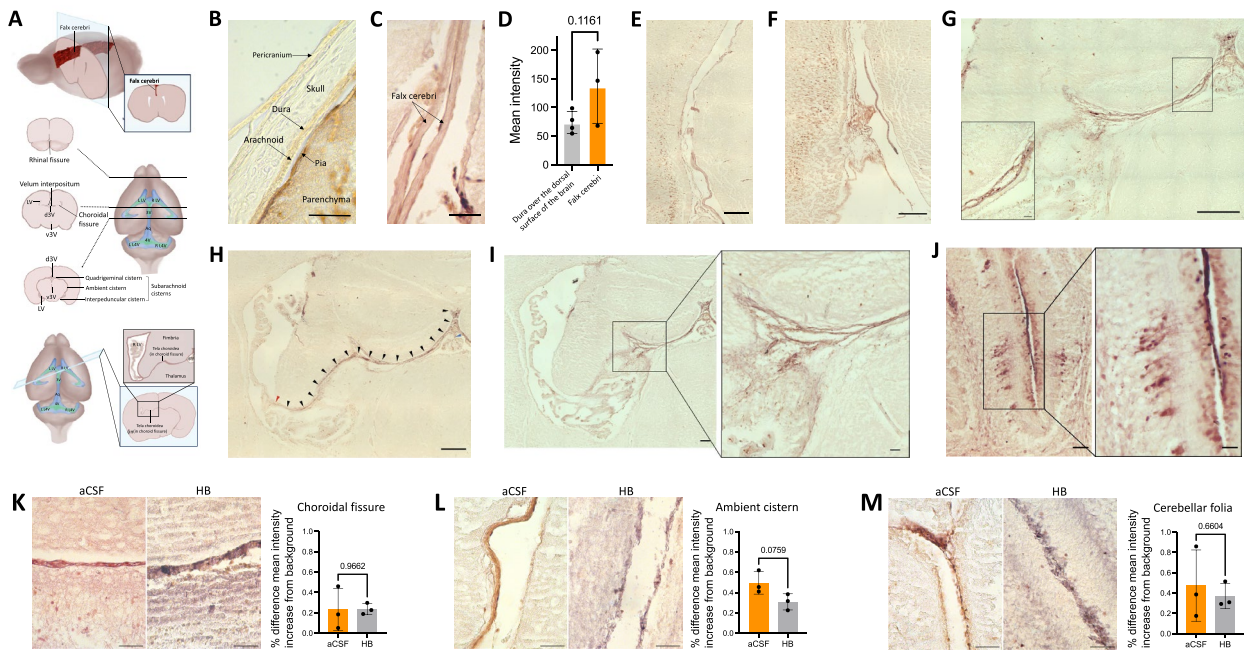


Fig. 5 Distribution of small CSF tracers within the intracranial meninges. **A** Schematic showing location of meningeal, cerebral ventricular, and choroid plexus (ChP) structures highlighted in **B–L**. **B** Representative histology showing small CSF tracer (brown) distribution through the decalcified skull, underlying meninges (dura, arachnoid, and pia maters), and parenchyma 10 min after 1.9-nm gold nanoparticle (AuNP) injection into the right lateral ventricle of P7 rodents. scalebar = 50 μ m. **C** Representative histology showing 1.9-nm AuNP distribution within the meningeal invaginations into the longitudinal fissure. The falx cerebri is labeled with a black arrow. C scalebar = 100 μ m. **D** Quantification of the mean intensity of 1.9-nm AuNP distribution within the dura mater over the surface of the brain compared to the falx cerebri. Data are mean \pm SD, n = 3 per group; Unpaired, two-tailed t-test. **E–G** Representative histology showing 1.9-nm AuNP distribution within the intracranial meninges of the ambient cistern (**E**), interpeduncular cistern (**F**), and choroidal fissure (**G**). **E** scalebar = 250 μ m, **F** scalebar = 250 μ m, **G** scalebar = 250 μ m. **H, I** Representative histology showing the path the tela choroidea takes through the choroidal fissure from the roof of the third ventricle to the ChP of the lateral ventricle (**H**) (black arrowheads), and the tela choroidea pia mater as it gives rise to the right lateral ventricle ChP (**H, I**) (red arrowhead, **H**; inset **I**). **H** scalebar = 250 μ m; **I** scalebar = 100 μ m, **I** inset scalebar = 50 μ m. **J** Representative histology of 1.9-nm AuNP distribution in the leptomeningeal invaginations into the folia of the cerebellum. **J** scalebar = 25 μ m, **J** inset scalebar = 10 μ m. **K–M**, 1.9-nm AuNP distribution in the choroidal fissure (**K**), ambient cistern (**L**), cerebellar folia (**M**), 10 min post-1.9-nm AuNP injection into the right lateral ventricle of rats with intraventricular hemorrhage-posthemorrhagic hydrocephalus (IVH-PHH, induced 72 h before AuNP injection with intraventricular hemoglobin (HB)) and aCSF control rats. **K–M** scalebars = 50 μ m, **J** scalebars = 250 μ m. Quantifications are also shown as mean \pm SD with unpaired two-tailed t tests, n = 3 animals per group. All data are representative of 3 rodents

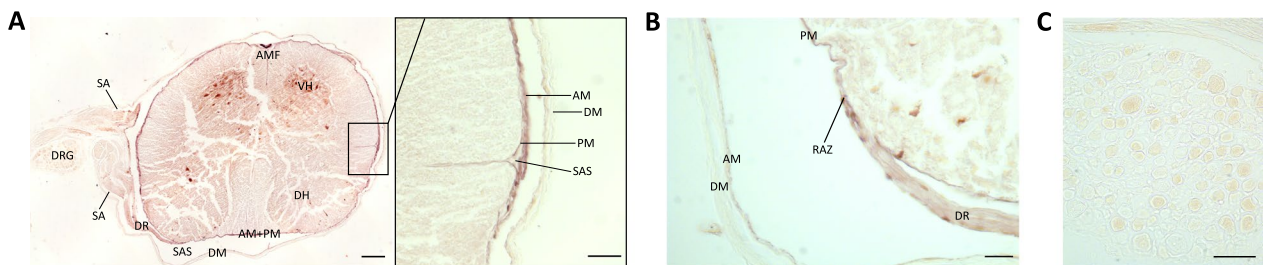


Fig. 6 Small CSF tracers predominantly circulate within the leptomeninges of the spinal cord and parenchyma. **A, B** Cross sectional histology showing small CSF tracer distribution (brown) in the spinal cord parenchyma, spine leptomeninges, and spine dura 10 min after 1.9-nm gold nanoparticle (AuNP) injection into the right lateral ventricle in P7 rodents. The anterior median fissure (AMF), ventral horn (VH), subarachnoid angle (SA), dorsal root ganglion (DRG), dorsal root (DR), pia mater (PM), subarachnoid space (SAS), dura mater (DM), root attachment zone (RAZ), and arachnoid mater (AM) are indicated. A scalebar = 1 mm, **A** inset scalebar = 25 μ m, **B** scalebar = 25 μ m. **C** High magnification histology showing 1.9-nm AuNP distribution in the dorsal root ganglion. Scalebar = 50 μ m. All data are representative of 3 rodents

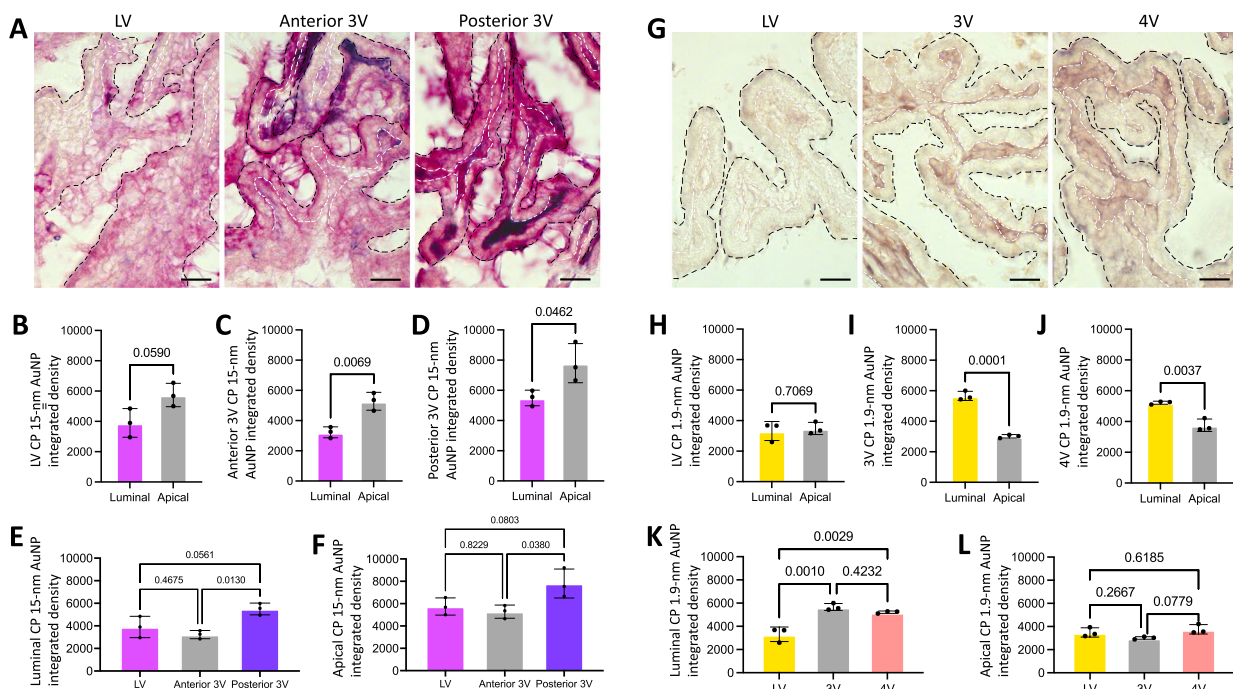


Fig. 7 CSF tracer distribution within the choroid plexus. **A** Representative histology of large CSF tracer distribution in the lateral ventricle (LV), anterior third ventricle (3V), and posterior 3V choroid plexuses (ChP) 4 h post-15-nm gold nanoparticle (AuNP) injection into the right LV of P7 rodents. Black dotted line indicates the apical surface of ChP epithelial cells, white dotted line indicates the basolateral surface of ChP epithelial cells. Scalebars = 25 μ m. **B–D** Quantification of 15-nm AuNP integrated density along the luminal and apical surfaces of the LV (**B**), anterior 3V (**C**), and posterior 3V (**D**) ChP. 15-nm AuNPs distributed along the apical surface of the anterior and posterior 3V ChP significantly more than the luminal surface. Data are mean \pm SD, $n = 3$ per group; Unpaired two-tailed t test. **E–F** Quantification of 15-nm AuNP distribution in the LV, anterior 3V, and posterior 3V ChP along the luminal (**E**) and apical (**F**) surfaces. There was significantly more 15-nm AuNP distribution on both the luminal and apical surfaces of the posterior 3V ChP compared to the anterior 3V ChP (**F**). Data are mean \pm SD, $n = 3$ per group; One-way ANOVA with post-hoc Tukey. All data are representative of 3 rodents. **G** Representative photomicrographs of small CSF tracer (brown) distribution in the LV, 3V, and fourth ventricle (4V) ChP 10 min post-1.9-nm gold nanoparticle AuNP injection into the lateral ventricle in P7 rodents. Black dotted line indicates the apical surface of ChP epithelial cells, white dotted line indicates the basolateral surface of ChP epithelial cells. Scalebars = 25 μ m. **H–J** Quantification of 1.9-nm AuNP integrated density between the luminal and apical surfaces of the LV (**H**), 3V (**I**), and 4V (**J**) ChP. There was significantly more AuNP distribution along the luminal surface of the 3V and 4V ChP compared to the apical surface. Data are mean \pm SD, $n = 3$ per group; Unpaired two-tailed t test. **K, L** Quantification and comparison of 1.9-nm AuNP distribution between the LV, 3V, and 4V ChP along the luminal (**K**) and apical surfaces (**L**). There was significantly more 1.9-nm AuNP distribution throughout the luminal 3V and 4V ChP compared to the LV, but no differences between regions on the apical ChP. Data are mean \pm SD, $n = 3$ per group; One-way ANOVA with post-hoc Tukey. All data are representative of 3 rodents

performed by measuring the straight-line distance from the outer surface of the dura to the inner surface of the dura on XRM images in FIJI.

RD/TMR quantifications

RD/TMR tracer distribution in Fig. 8 was quantified in FIJI by selecting 3 random regions from each layer of tissue that was identified in Fig. 8E (CRABP2+/RALDH2+, CRABP2-/RALDH2-, CRABP2 \pm /RALDH2-, cortex parenchyma) and measuring the mean intensity of fluorescence on the magenta/red channel in FIJI. The three regions were averaged to obtain one measurement per layer of tissue per animal. This was repeated across 4

separate animals. Averaged values were compared with statistical analyses.

Sample preparation for meninges analysis using gold nanoparticle-enhanced X-ray microtomography

After intracardial perfusion sacrifice 10 min post-1.9-nm AuNP injection and 4 h post-15-nm AuNP injection, the entire rodent body was placed in 4% paraformaldehyde at 4 $^{\circ}$ C overnight, embedded in 2% agarose, and imaged within 72 h of sacrifice with a Zeiss Versa 520 X-ray microscope (Carl Zeiss Imaging, White Plains, NY) using a 0.4 \times flat panel detector as previously described [37]. The X-ray source was tuned to 50 kV at 4W to optimally excite gold particles.

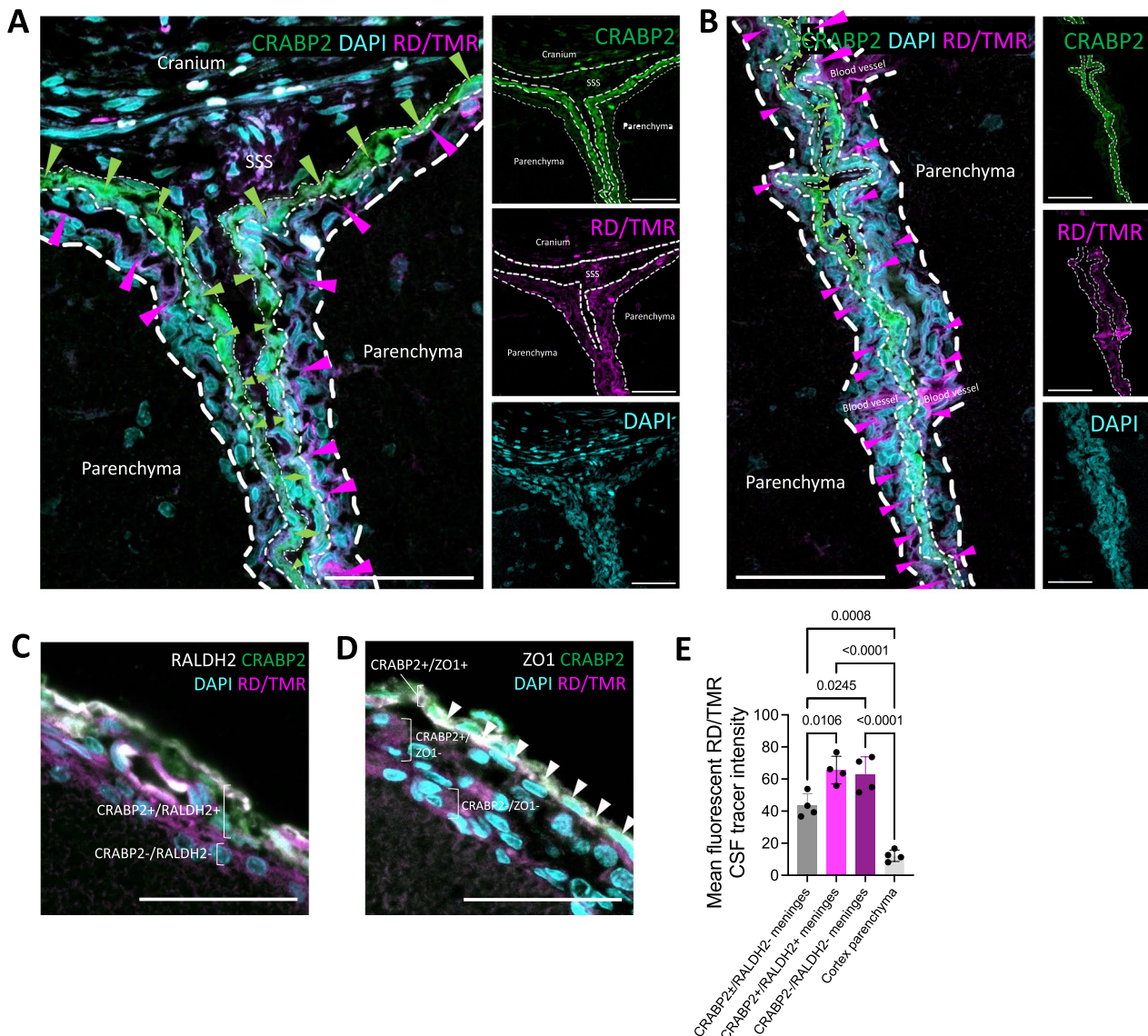


Fig. 8 Immunofluorescent co-localization of small fluorescent CSF tracers with meningeal fibroblast markers. **A, B**, Representative photomicrograph of 3 kDa Red Dextran Tetramethylrhodamine (RD/TMR) (magenta, magenta arrowheads) distribution along the meninges around **(A)** and within **(A, B)** the longitudinal fissure 10 min after intraventricular injection into the right lateral ventricle in P7 rodents. RD/TMR distribution is primarily within the meningeal layer(s) inferior to a cellular retinoic acid binding protein 2 (CRABP2) (green, green arrowheads)-positive layer (inferior layer identified as the pia mater), with additional RD/TMR co-localization with the CRABP2+ layer (identified as the arachnoid mater). The putative border between the pia mater and underlying parenchyma is indicated with thick white dashed line; the pia and arachnoid are separated by the medium white dashed line, and the arachnoid and dura (falx) are separated by the thin white dashed line. Very little RD/TMR is seen medial/superior to the CRABP2+ layer (dura mater). **A, B** scalebars = 50 μ m. **C, D** Representative photomicrographs of RD/TMR distribution in the meninges over the dorsal surface of the brain and CRABP2, retinaldehyde dehydrogenase 2 (RALDH2), and zonula occludens 1 (ZO-1) staining. RD/TMR co-localized with a CRABP2+/RALDH2+ layer (arachnoid mater), in addition to the inferiorly adjacent CRABP2-/RALDH2- layer (pia mater) **(C)**. RD/TMR distribution was inferior to the CRABP2+/ZO-1+ layer (arachnoid barrier cell layer), suggesting it localizes to the arachnoid and pia maters **(D)**. **E**, Quantification of RD/TMR mean intensity in CRABP2+/RALDH2- meninges (dura), CRABP2+/RALDH2+ meninges (arachnoid), CRABP2-/RALDH2- meninges (pia), and the parenchyma of the cortex. There was significantly less RD/TMR in the dura and cortex parenchyma compared to the pia and arachnoid. Data are mean \pm SD, n = 4 per group; One-way ANOVA with post-hoc Tukey. All data are representative of 4 rodents

Approximately 1600 projections were acquired and reconstructed, and tomograms were visualized in Zeiss XM3DViewer 1.2.8 (Carl Zeiss Imaging, White Plains, NY). Processed images were systematically reviewed in FIJI (Version 2.3.0).

AuNP quantifications from XRM images

For standardization, processed images from 1.9-nm and 15-nm AuNP-XRM scans were numbered by their location relative to bregma so the location of the selected images was consistent across rodents. One image per rodent (3 rodents total for 1.9-nm AuNP-XRM and 3 rodents total for 15-nm AuNP-XRM) at the level of the inferior colliculus was selected for quantification in Figs. 1G, H and 4F, G and the corresponding XRM raw data file was opened in FIJI (version 2.3.0/1.53q). The mean gray intensity of three random regions within each anatomic ROI (dura, arachnoid, and pia) were calculated using FIJI/ImageJ and averaged to obtain one mean gray intensity measurement per anatomic ROI per rodent. The mean gray intensity of the agarose background was also obtained for each image and the percent change between the mean intensity of the anatomic ROIs and the mean intensity of the agarose background was calculated for standardization. A similar protocol was followed for the quantifications shown in Figs. 2H–J and 5K–M, however the XRM raw data files were manually selected for each region.

To quantify AuNP intensity in the pia, we selected regions of interest adjacent to the brain tissue (region of very low to no enhancement) and subjacent to the SAS (region of very high enhancement). To quantify the AuNP intensity in the arachnoid, we selected regions of interest adjacent to the SAS (region of very high enhancement) and subjacent to the dura (region of medium intensity enhancement). As a general guide to distinguish the SAS from the tissue layers of the pia and arachnoid maters, the pia mater was primarily identified as a thin rim of slightly brighter (relative to the SAS) enhancement that closely approximated the brain parenchyma tissue, and the arachnoid was identified as a thin rim of slightly brighter (relative to the SAS, but less bright than the pia) enhancement superior to the SAS. When there was more ambiguity and the pia and arachnoid could not be identified on the basis of brighter enhancement relative to the SAS, we scrolled through individual serial slices of the XRM image so that we could follow the course of blood vessels and nerves and identify a “break” or invagination in the pia as they entered/exited the brain parenchyma into the SAS, or a “break” or invagination in the arachnoid as the blood vessels and nerves exited/entered the SAS to the dura. We could subsequently follow these

invaginations to identify the layers of tissue which form the invaginations to identify the pia and arachnoid respectively.

Meningeal wholemounts

4 hours post-15 nm AuNP injection and 10 minutes post-1.9 nm AuNP injection as previously described, rodents were deeply anesthetized with isoflurane and perfused with 10 mL of ice-cold PBS followed by 10 mL of 4% paraformaldehyde at 4 °C. The cranium and spinal column were removed from the animal and severed at the brainstem. The cranial dura was removed by adapting a previously reported protocol [10, 18]. Curved micro scissors were inserted into the foramen magnum and used to remove the top of the skull without damaging the underlying pia and brain tissue. The skullcap and brain were separately incubated in 4% PFA overnight. The dura was dissected from the bone while the leptomeninges (pia and arachnoid maters) were carefully peeled away from the brain surface.

The spinal cord was isolated from the vertebrae by using curved micro scissors to sever the pedicles bilaterally before removing the spinal cord with forceps. The dorsal half of the spinal cord was secured with forceps and its adherent dura, which appeared as a loose-hanging translucent layer, was gently peeled away and mounted on a glass slide. The dorsal leptomeninges were gently peeled away from the underlying parenchyma. This was repeated on the ventral half of the spinal cord. Wholemounts were transferred onto a glass slide, air dried, and mounted with Permunt mounting medium (#SP15-100, Thermo Fisher Scientific, Waltham, MA).

Statistical analysis

Statistical methods were not used to recalculate or pre-determine sample sizes. Associations between two continuous variables were assessed using an unpaired T-test, and associations between more than two continuous variables were assessed using a one-way ANOVA with post-hoc Tukey. All tests were 2-tailed, and p-values of less than 0.05 were considered statistically significant with all p values displayed on the graphs or reported in the corresponding figure legend. All analyses were performed using Microsoft Office Excel (Version 16.36) or Graph-Pad Prism (Version 9.0.0).

Results

Transport of large CSF solutes: brain surface

We examined differential CSF handling of large CSF tracers by the cranial leptomeninges (pia and arachnoid maters) and pachymeninges (dura mater) 4 h after intraventricular injection of 15-nm AuNPs, which appear

magenta on gross visualization and light microscopy. Similar to the findings in previously published analyses of tracer distribution in the dura [10], 15-nm AuNP circulation within the dura, which was morphologically identified as the layer(s) immediately inferior to the skull, was restricted to the parasagittal and transverse sinus regions with only small amounts of 15-nm AuNP distribution in non-sinus regions (Fig. 1B–D, Additional file 1: Fig. S1A). At midline, the dura mater over the inferior colliculus was significantly thicker than the dura mater over the cortex more anteriorly and the cerebellum posteriorly (Fig. 1E).

In contrast to the dura, 15-nm AuNPs distributed uniformly throughout the leptomeninges (Fig. 1B–D). When the leptomeninges were removed, the underlying brain surface had minimal AuNP distribution, with only punctate evidence of AuNPs around the penetrating blood vessels (Additional file 1: Fig. S1B). Leptomeningeal wholemounts of the area immediately adjacent to the middle cerebral artery (MCA) supported our histologic observations of 15-nm AuNP distribution within the leptomeningeal tissue (Additional file 1: Fig. S1B).

We also obtained high-resolution whole-brain images using X-ray microtomography (XRM), which allowed for ex-vivo visualization of the meninges without dissection (Fig. 1F). Similar to what we qualitatively observed with wholemounts and histology, XRM revealed there was significantly more 15-nm AuNP distribution within the pia mater compared to the dura mater and a trend towards increased 15-nm AuNP distribution in the arachnoid mater compared to the dura mater (Fig. 1G). 15-nm AuNPs in the pia did not appear to travel inferiorly into the adjacent parenchyma (Fig. 1H), as there was significantly higher 15-nm AuNP intensity in the pia compared to the parenchyma.

Meningeal handling of large CSF solutes within the brain

On cross section, we did not observe significant differences in 15-nm AuNP distribution between non-sinus-associated dura over the dorsal surface of the brain and the falx cerebri (Fig. 2B–D) [19]. We identified widespread 15-nm AuNP circulation through the leptomeninges of the perimesencephalic cisterns (Fig. 2E), including the quadrigeminal, ambient, and interpeduncular cisterns, and the rhinal fissure (Fig. 2F). In contrast to the meninges at the surface of the brain (Fig. 1H), there appeared to be CSF trafficking from the intracranial meninges into the adjacent parenchyma, as brain tissue adjacent to the perimesencephalic cisterns had a gradient of diffuse 15-nm AuNP distribution extending from the cisterns into the parenchyma (Fig. 2E). 15-nm AuNPs also circulated throughout the pia mater traversing the CSF spaces intracranially, including the tela choroidea

in the roof of the 3 V and velum interpositum (Fig. 2G). These patterns of 15-nm AuNP distribution through the tela choroidea were similar to a previously described pattern of superficial siderosis and has implications for direct communication between the ventricles outside the ependymal-lined CSF cavities [20, 21]. There were no differences in the intensity of CSF solute distribution within the intracranial meninges after IVH-PHH (Fig. 2H–J).

Meningeal handling of large CSF solutes within the spine

We also evaluated large CSF tracer distribution within the spine meninges. Unlike the cranial dura that adheres to the cranium during dissection, the spinal dura did not adhere to the vertebrae and was dissected away from the leptomeninges (Fig. 3A). The pia and arachnoid were peeled back from the underlying parenchyma in one piece (Fig. 3B, C).

Similar to the cranial meninges, we did not observe widespread large CSF solute distribution within the spinal dura, except for diffuse AuNPs along the lower thoracic and lumbar nerve rootlets and roots exiting the spinal cord in the lower thoracic and lumbar regions (Fig. 3A). In contrast to the minimal large CSF solute handling by the dura, we observed widespread large CSF solute circulation through the dorsal and ventral leptomeninges that outlined the structure of the median fissures and nerve roots (Fig. 3B–D). Leptomeningeal 15-nm AuNP distribution was present in higher concentrations around the nerve roots, with additional diffuse circulation within the nerve roots (Fig. 3E–G). On cross section of the spine, 15-nm AuNPs were seen in the arachnoid mater, pia mater, anterior median fissure, central canal, dorsal root, and root attachment zone (Fig. 3H–K).

Meningeal handling of small CSF solutes on the surface of the brain and within the brain

1.9-nm AuNP-enhanced XRM in conjunction with histology was used to evaluate small CSF tracer distribution within the dura, arachnoid, and pia. 1.9-nm AuNPs appeared brown on gross visualization and light microscopy. Similar to our findings with 15-nm AuNPs, non-sinus associated dura mater had significantly less 1.9-nm AuNP distribution compared to the arachnoid and pia maters 10 min post-intraventricular 1.9-nm AuNP injection (Fig. 4A–G). While there was no overall significant difference in small CSF tracer handling between the dura over the dorsal surface of the brain and the falx cerebri, the mean intensity of 1.9-nm AuNP distribution in the falx cerebri in two out of three rodents was greater in magnitude than the mean intensity of 1.9-nm AuNP distribution in the dura over the dorsal surface of the brain in all rodents quantified (Fig. 5B–D).

We also evaluated small CSF tracer handling in the intracranial leptomeninges using histology. 10 min after intraventricular injection of 1.9-nm AuNPs, there was notable 1.9-nm AuNP circulation in the leptomeninges of the perimesencephalic cisterns, including the ambient and interpeduncular cisterns, as well as the choroidal fissure (Fig. 5E–G). This was similar to the large CSF tracer distribution patterns observed 4 h post-15-nm AuNP injection. 1.9-nm AuNPs were also observed in the pia mater of the tela choroidea in the choroidal fissure (Fig. 5G–I), and at the entry of the tela choroidea pia mater into the right LV ChP (Fig. 5I). This was akin to the 15-nm AuNP distribution seen in the dorsal 3V and velum interpositum. There was also 1.9-nm AuNP circulation in the pia mater in the folia of the cerebellum (Fig. 5J). No significant differences in small CSF tracer distribution within the intracranial meninges were observed after IVH-PHH (Fig. 5K–M).

Meningeal handling of small CSF solutes within the spine

Similar to what we observed with large CSF solutes, there was broad small CSF solute distribution through the spinal leptomeninges 10 min after intraventricular injection, but not within the dura mater (Fig. 6A). On cross section, 1.9-nm AuNPs were concentrated in the anterior median fissure, ventral horn, dorsal root, and root attachment zone (Fig. 6A, B). 1.9-nm AuNPs were also seen within the invaginations around penetrating blood vessels (Fig. 6A). Notably, 1.9-nm AuNPs were present in the cell bodies of the dorsal root ganglia (Fig. 6A, C); the distribution among the cell bodies was not homogenous, with some cell bodies taking up more AuNPs than others (Fig. 6C).

CSF solute handling by the choroid plexus

Given the close developmental relationship between the tela choroidea and ChP, we evaluated ChP handling of large and small CSF solutes. Large solutes were present in the LV, anterior 3V, and posterior 3V ChPs 4 h after intraventricular injection (Fig. 7A). There was significantly more apical than luminal 15-nm AuNP distribution in the anterior and posterior 3V ChPs, but no difference in the LV ChP (Fig. 7B–D). When comparing 15-nm AuNP distribution between the LV, anterior 3V, and posterior 3V ChP, there was significantly more 15-nm AuNP distribution in the posterior 3V ChP compared to the anterior 3V ChP 4 h post-injection (Fig. 7E, F).

In contrast to large CSF solutes, there was significantly decreased small CSF solute (1.9-nm) distribution on the apical side in the 3V and 4V ChPs compared to

the luminal side 10 min post-injection, but not in the LV ChP (Fig. 7G–J). There was also increased 1.9-nm AuNP distribution on the luminal side of the 3V and 4V ChPs compared to the LV ChP (Fig. 7K), however no difference was observed on the apical side between the three locations (Fig. 7L).

Fluorescent CSF tracer colocalization with meningeal fibroblast markers

To verify the identity of the meningeal layers interacting with CSF tracer, we injected 3 kDa fluorescent CSF tracer RD/TMR into the right LV to allow for tracer colocalization with meningeal fibroblast markers including the arachnoid fibroblast markers retinaldehyde dehydrogenase 2 (RALDH2) [13], the arachnoid and dural fibroblast marker cellular retinoic acid binding protein 2 (CRABP2) [13], and the tight junction protein zonula occludens 1 (ZO-1). RD/TMR co-localized with layers of cells that were strongly positive for CRABP2 and RALDH2, and another layer that was CRABP2–/RALDH2– located superior to the brain parenchyma but inferior to the CRABP2+/RALDH2+ layer (Fig. 8A–C). Both of these layers were inferior to a CRABP2+/ZO-1 layer (Fig. 8D), suggesting they represent the arachnoid and pia maters. Within cross sections of the falx cerebri, there were additional layers of tissue medial to the strongly CRABP2+ layer that largely did not have RD/TMR distribution that likely represented the dura mater (Figs. 8A, B), which is anatomically medial to the arachnoid, pia, and parenchyma in the midline. There was a small region within the dura mater that had punctate RD/TMR distribution that likely represented the superior sagittal sinus (SSS). The CRABP2+/RALDH2+ (arachnoid) and CRABP2–/RALDH2– (pia) layers had significantly more RD/TMR CSF tracer than the more superior CRABP2±/RALDH2– layer (dura) outside of the sinus areas (Fig. 8E), which is consistent with our observations with AuNPs that relied on morphologic identification of the meningeal layers.

Discussion

Patterns of CSF distribution through and interaction with the cellular components of the meninges, particularly the developing intracranial leptomeninges (pia and arachnoid maters) and spine meninges are not well known [22]. In this study, we report the distribution of large and small CSF tracers within the meningeal and ventricular networks during the postnatal time period. We show that after injection into the LV, small and large CSF tracers distribute through the cranial and spinal leptomeninges, notably in the perimesencephalic cisterns and tela choroidea. In the ChP, small tracers were localized to the

lumen, with differential distribution between the ventricles; the 4V and 3V ChP had significantly more tracer than the LV. Large tracers were localized to the apical ChP with significantly more tracer in the posterior 3V compared to the anterior 3V.

By closely analyzing the macroscopic distribution of CSF tracers through the meninges and ChP, we specifically hope to call attention to the role of structures outside the arachnoid granulations and dura in CSF solute distribution, especially during the neonatal and postnatal time period. The differential handling of CSF tracers by the dura and leptomeninges may suggest that the different layers of the meninges have distinct roles in CSF handling. The regional differences in small CSF tracer handling between the dura over the surface of the brain and the dura within the interhemispheric invagination (ie. the falx cerebri) in two out of three rodents suggest that the slightly higher amounts of small CSF tracer within the falx cerebri may be secondary to the falx cerebri playing a role in mediating CSF-dural sinus interactions. Specifically, the falx cerebri is in unique proximity to the superior sagittal sinus. The inferior sagittal sinus courses through the lower boundary of the falx cerebri, suggesting the falx cerebri may provide a local environment extending down the depth of the cortex in which CSF, proteins, and molecules from the interstitial fluid (ISF) and brain parenchyma are able to be trafficked into the parasagittal meningeal lymphatics to allow for ongoing CSF handling and immune monitoring, particularly in older animals with functional meningeal lymphatics [10, 23–28]. Further investigations should focus on the nature and rate of CSF transport including tracer, protein, and other molecules into the falx compared to other dural regions.

The perimesencephalic cisterns are filled with cerebrospinal fluid, surround the midbrain, and include the ambient, crural, interpeduncular, and quadrigeminal cisterns [29]. The lack of significant changes in leptomeningeal transport of CSF solutes within and around these cisterns after IVH-PHH may have implications for meningeal handling and transport of neurotoxic blood breakdown products that are released into the CSF after hemorrhage (including hemoglobin, heme, and iron [17]), and other blood products such as platelets, fibrin, and thrombin which have also previously been linked to brain injury after IVH [30–33]. Hemoglobin and iron specifically are known to be necessary for the pathogenesis of PHH after IVH [17], and preservation of meningeal CSF solute pathways may allow for transport of iron to distant locations of the brain via the perimesencephalic and other cisterns. The perimesencephalic cisterns separate two functionally-distinct regions—the hippocampus and the midbrain. This, in conjunction with the results of

our present study showing diffuse 15-nm AuNP movement into only the hippocampal side of the quadrigeminal, and ambient cisterns, but not the midbrain, suggest that these cisterns may serve to facilitate a regionalized CSF-brain parenchyma cross talk [34–37]. Alternatively, their location in between the LV and 3V may serve as a potential route for inter-ventricular CSF transport and communication [21]. While we did not see any significant differences in tracer distribution within the meninges of these cisterns after IVH-PHH, it is possible there are functional differences allowing increased/decreased CSF solute transport from the cisterns into the adjacent parenchyma that should be explored in future studies. Additionally, the meninges actively mature during postnatal development, undergoing various molecular, structural, and functional changes [13, 38–42]. Future studies should explore the effects of inducing IVH-PHH at earlier or later stages of postnatal development, as developmental stage may differentially affect the extent to which CSF solutes are able to distribute across the meninges as the meninges mature.

In addition to the perimesencephalic cisterns, one particularly intriguing yet understudied intracranial meningeal structure is the tela choroidea, a thin region of pia mater adherent to the underlying 4V ependyma [43–48]. In the 3V, the tela choroidea forms the roof of the ventricle and superimposes upon itself to form the velum interpositum, which lies between the internal cerebral veins and contains cerebrospinal fluid [43, 45, 47, 49, 50]. The 3V tela choroidea is continuous with the LV via the choroidal fissure. The tela choroidea also gives rise to the ChP in each of the brain's ventricles. The tela choroidea has been purported to have a role in allowing CSF to be recirculated into the ventricular system but has otherwise been sparsely studied in the context of CSF circulation [20, 51, 52]. In this study, we report that 1.9-nm AuNPs were found predominantly in the luminal side of the 3V and 4V ChP as soon as 10 min post-injection. There was significantly less luminal 1.9-nm AuNP in the LV ChP compared to the 3V and 4V. In addition, there was significantly less apical compared to luminal 1.9-nm AuNP distribution in all of the ventricles, suggesting that the 1.9-nm AuNPs were not being shuttled across the ChP epithelial cells into the lumen, but rather directly transported along the luminal pia mater. It is possible that the first point of 1.9-nm AuNP entry to the ChP is through the tela choroidea of the 4V or the roof of the 3V and eventually the choroidal fissure and LV ChP. A previous study on experimental hydrocephalus in primates and dogs posited that CSF traveled to the ventricles from the cisterns via the tela choroidea [52, 53]. Other studies have indicated that CSF may be transported across a normally functioning tela choroidea into the ChP and

ventricles as a regular aspect of brain physiology [20, 51]. The results of this present study support these findings and build upon previous studies implicating the ChP in direct CSF solute transport [54, 55]. Future studies should map the timeline of CSF tracer distribution along the tela choroidea and LV, 3V, and 4V ChP *in vivo*.

While not as well-studied in the neonatal and postnatal time period, there has been a long-standing body of literature suggesting CSF tracers injected into the ventricles and cisterns of adult and aged animals are eventually drained into the lymphatic system [10, 12, 56–69]. There are several proposed routes by which this occurs: (1) perivascular and perineural routes into extracranial and extraspinal soft tissue, after which they are absorbed into the lymphatic system, and (2) dural meningeal lymphatics [10, 57]. In the latter theory, it is not entirely clear how solute movement bridges the CSF spaces (SAS) and dura (where meningeal lymphatics are located), as CSF solutes would presumably have to pass through the blood-CSF barrier posed by the outer arachnoid which separates the SAS from the dura. The results in this study suggest that CSF tracer in the SAS may not cross the arachnoid layer of the meninges to enter into the dura in great quantities, a finding which is supported by previous literature [70–75]. This finding calls the role of dural meningeal lymphatics in CSF outflow during the postnatal period into question, suggesting alternative routes of CSF outflow exist. One caveat is that the experiments in this study were conducted in postnatal rodents, a time during which meningeal lymphatics may not be fully developed [28]. Future studies in adult rodents should investigate the nature of these functional connections to elucidate the specific route by which CSF solutes are transported from the CSF into the dural meningeal lymphatics. Future studies should also investigate in parallel alternative routes of CSF outflow which may play a greater role in CSF drainage than the dural meningeal lymphatics, including CSF outflow along perivascular and perineural subarachnoid spaces into extracranial lymphatics of the skull base [12].

One limitation of this study is that our investigations were conducted *ex vivo*, which may impact the structure and presence of CSF spaces such as the SAS. Similarly, while decalcification with EDTA and HCl allowed for visualization of the skull, meninges, and brain in approximation with each other, it resulted in disfiguration of the skull over the dorsal convexities. Our investigation was based on rodents, animals in which the presence, morphology, and function of arachnoid villi have been debated. Additionally, the conclusions in this study were made in part on the basis of images obtained using light microscopy; future studies should examine CSF tracer distribution at an ultrastructural level in the regions we called out in this present study. Finally, the animal (rat)

we used for this study is lissencephalic, which may affect the leptomeningeal distribution of CSF tracers in the cerebrum as the pia mater follows the invaginations produced in animals with gyri and sulci. In the cerebellum, which retains its sulci and gyri in the rodent brain, there was an abundance of CSF tracer in the pia mater invaginations into the folia. Repeating these experiments in organisms with gyri and sulci, such as pigs or ferrets, may show similar patterns of tracer in the leptomeninges over the cerebral cortex.

Conclusion

We present a CNS-wide map of meningeal handling of large and small CSF solutes in the neonatal brain and spine. Intracranial leptomeninges, particularly the tela choroidea in the 4V and at the roof of the 3V, are an important area for CSF circulation and future studies should be performed to characterize mechanisms of CSF transport in these areas. Differential ChP distribution of tracers by ventricle and between the luminal and apical surfaces suggests region-specific functions in facilitating CSF flow. Finally, we show that meningeal handling of both large and small CSF solutes is mediated primarily by the pia and arachnoid in young animals.

Abbreviations

AuNP	Gold nanoparticle
ChP	Choroid plexus
CNS	Central nervous system
CSF	Cerebrospinal fluid
ISF	Interstitial fluid
IVH	Intraventricular hemorrhage
PHH	Posthemorrhagic hydrocephalus
RD/TMR	Red dextran tetramethylrhodamine
SAS	Subarachnoid space
3V	Third ventricle
4V	Fourth ventricle
LV	Lateral ventricle

Supplementary Information

The online version contains supplementary material available at <https://doi.org/10.1186/s12987-023-00503-7>.

Additional file 1. Supplementary methods and Supplementary Figure 1.

Acknowledgements

Not applicable.
Jennifer M. Strahle: Lead contact.

Author contributions

SP designed and performed experiments and wrote the manuscript; JK analyzed data and wrote the manuscript; GMK analyzed data and assisted with experimental procedures; GLH analyzed data and assisted with experimental procedures; AOA assisted with experimental procedures, SK assisted with experimental procedures, DD performed experiments; SR performed experiments; JMS designed experiments, supervised the work, and wrote the manuscript.

Funding

This work was funded by the National Institutes of Health (R01 NS110793 to J.M.S.), Rudy Schulte Research Institute (J.M.S.), K12 Neurosurgeon Research Career Development Program (J.M.S.), the Hydrocephalus Association (J.M.S.), McDonnell Center for Systems Neuroscience at Washington University in St. Louis (J.M.S.), the Children's Discovery Institute (J.M.S.), and the Washington University in St. Louis Center for Cellular Imaging also known as WUCCI (J.M.S.). XRM imaging was performed with a Zeiss Xradia 520 X-ray Microscope at WUCCI, which is supported by Washington University in St. Louis School of Medicine and the NIH (OD021694). Figures were created with BioRender.com.

Availability of data and materials

The datasets generated during and/or analysed during the current study are available from the corresponding author on reasonable request.

Declarations

Ethics approval and consent to participate

All experiments were approved by the Institutional Animal Care and Use Committee of Washington University (protocol #22-0614). Research including human participants/material/data were not used in this article.

Consent for publication

All authors of the manuscript have read and consent to the publication of this manuscript. The authors affirm that the article is original and is not under consideration for publication/has not been published by another journal.

Competing interests

The authors have no relevant competing interests to disclose.

Author details

¹Department of Neurosurgery, Washington University School of Medicine, Washington University in St. Louis, St. Louis, MO 63110, USA.

Received: 10 August 2023 Accepted: 12 December 2023

Published online: 08 January 2024

References

- Rasmussen MK, Mestre H, Nedergaard M. Fluid transport in the brain. *Physiol Rev.* 2022;102:1025–151. <https://doi.org/10.1152/physrev.00031.2020>.
- Weed LH. Meninges and cerebrospinal fluid Anatomy Lrxll.
- Cserr HF. Physiology of the choroid plexus. *Physiol Rev.* 1971;51:273–311. <https://doi.org/10.1152/physrev.1971.51.2.273>.
- Quinton PM, Wright EM, Tormey JM. Localization of sodium pumps in the choroid plexus epithelium. *J Cell Biol.* 1973;58:724.
- Dohrmann GJ. The choroid plexus: a historical review. *Brain Res.* 1970;18:197–218.
- Ellis DZ, Nathanson JA, Sweadner KJ. Carbachol inhibits Na(+)-K(+)-ATPase activity in choroid plexus via stimulation of the NO/cGMP pathway. *Am J Physiol Cell Physiol.* 2000;279: C1685.
- Lindvall M, Owman C. Autonomic nerves in the mammalian choroid plexus and their influence on the formation of cerebrospinal fluid. *J Cereb Blood Flow Metab.* 1981;1:245–66.
- Cushing H. Studies on the cerebro-spinal fluid: I. Introduction. *J Med Res.* 1914;31:1.
- Siegenthaler JA, Pleasure SJ. We have got you "covered": how the meninges control brain development. *Curr Opin Genet Dev.* 2011;21:249.
- Louveau A, Smirnov I, Keyes TJ, Eccles JD, Rouhani SJ, Peske JD, et al. Structural and functional features of central nervous system lymphatic vessels. *Nature.* 2015;523:7560.
- Ahn JH, Cho H, Kim JH, Kim SH, Ham JS, Park I, et al. Meningeal lymphatic vessels at the skull base drain cerebrospinal fluid. *Nature.* 2019;572:62–6.
- Koh L, Zakharov A, Johnston M. Integration of the subarachnoid space and lymphatics: is it time to embrace a new concept of cerebrospinal fluid absorption? *Cerebrospinal Fluid Res.* 2005;2:6.
- DeSisto J, O'Rourke R, Jones HE, Pawlikowski B, Malek AD, Bonney S, et al. Single-cell transcriptomic analyses of the developing meninges reveal meningeal fibroblast diversity and function. *Dev Cell.* 2020;54:43–59.e4.
- Strahle J, Garton HJL, Maher CO, Muraszko KM, Keep RF, Xi G. Mechanisms of hydrocephalus after neonatal and adult intraventricular hemorrhage. *Transl Stroke Res.* 2012;3:25.
- Ramagiri S, Pan S, DeFreitas D, Yang PH, Raval DK, Wozniak DF, et al. Deferoxamine prevents neonatal posthemorrhagic hydrocephalus through choroid plexus-mediated iron clearance. *Transl Stroke Res.* 2022;14:704–22.
- Miller BA, Pan S, Yang PH, Wang C, Trout AL, DeFreitas D, et al. Modeling neonatal intraventricular hemorrhage through intraventricular injection of hemoglobin. *J Vis Exp.* 2022. <https://doi.org/10.3791/63345>.
- Strahle JM, Garton T, Bazzi AA, Kilaru H, Garton HJL, Maher CO, et al. Role of hemoglobin and Iron in hydrocephalus after neonatal intraventricular hemorrhage. *Neurosurgery.* 2014;75:696.
- Louveau A, Filiano AJ, Kipnis J. Meningeal whole mount preparation and characterization of neural cells by flow cytometry. *Curr Protoc Immunol.* 2018;121:e50.
- Glinksi O, Huxley VH, Xie L, Bunyak F, Palaniappan K, Glinksi V. Complex non-sinus-associated pachymeningeal lymphatic structures: interrelationship with blood microvasculature. *Front Physiol.* 2019;10:1364.
- Maurizi CP. Superficial siderosis of the brain: roles for cerebrospinal fluid circulation, iron and the hydroxyl radical. *Med Hypotheses.* 1996;47:261.
- Park JH, Park YS, Suk JS, Park SW, Hwang SN, Nam TK, et al. Cerebrospinal fluid pathways from cisterns to ventricles in N-butyl cyanoacrylate-induced hydrocephalic rats: laboratory investigation. *J Neurosurg Pediatr.* 2011;8:640.
- Bedussi B, Van Der Wel NN, de Vos J, Van Veen H, Siebes M, VanBavel E, et al. Paravascular channels, cisterns, and the subarachnoid space in the rat brain: a single compartment with preferential pathways. *J Cereb Blood Flow Metab.* 2017;37:1374.
- Louveau A, Herz J, Alme MN, Salvador AF, Dong MQ, Viar KE, et al. CNS lymphatic drainage and neuroinflammation are regulated by meningeal lymphatic vasculature. *Nat Neurosci.* 2018;21:1380.
- Rustenhoven J, Drieu A, Mamuladze T, de Lima KA, Dykstra T, Wall M, et al. Functional characterization of the dural sinuses as a neuroimmune interface. *Cell.* 2021;184:1000–1016.
- da Mesquita S, Louveau A, Vaccari A, Smirnov I, Cornelison RC, King-smore KM, et al. Functional aspects of meningeal lymphatics in ageing and Alzheimer's disease. *Nature.* 2018;560:7717.
- da Mesquita S, Papadopoulos Z, Dykstra T, Brase L, Farias FG, Wall M, et al. Meningeal lymphatics affect microglia responses and anti-Aβ immunotherapy. *Nature.* 2021;593:255–60.
- Izen RM, Yamazaki T, Nishinaka-Arai Y, Hong YK, Mukouyama YS. Postnatal development of lymphatic vasculature in the brain meninges. *Dev Dyn.* 2018;247:741.
- Antila S, Karaman S, Nurmi H, Airavaara M, Voutilainen MH, Mathivet T, et al. Development and plasticity of meningeal lymphatic vessels. *J Exp Med.* 2017;214:3645.
- Ulm AJ, Tanriover N, Kawashima M, Campero A, Bova FJ, Rhoton AL, et al. Microsurgical approaches to the perimesencephalic cisterns and related segments of the posterior cerebral artery: comparison using a novel application of image guidance. *Neurosurgery.* 2004;54:1313–28.
- Gao F, Liu F, Chen Z, Hua Y, Keep RF, Xi G. Hydrocephalus after intraventricular hemorrhage: the role of thrombin. *J Cereb Blood Flow Metab.* 2014;34:1070.
- Botfield H, Gonzalez AM, Abdullah O, Skjolding AD, Berry M, Mcallister JP, et al. Decorin prevents the development of juvenile communicating hydrocephalus. *Brain.* 2013;136:2842.
- Whitelaw A, Christie S, Pople I. Transforming growth factor-β1: a possible signal molecule for posthemorrhagic hydrocephalus? *Pediatr Res.* 1999;46:576.
- Aojuola A, Botfield H, McAllister JP, Gonzalez AM, Abdullah O, Logan A, et al. Diffusion tensor imaging with direct cytopathological validation: characterisation of decorin treatment in experimental juvenile communicating hydrocephalus. *Fluids Barriers CNS.* 2016;13:9.

34. Zappaterra MW, Lehtinen MK. The cerebrospinal fluid: regulator of neurogenesis, behavior, and beyond. *Cell Mol Life Sci.* 2012;69:2863–78.
35. Fame RM, Lehtinen MK. Emergence and developmental roles of the cerebrospinal fluid system. *Dev Cell.* 2020;52:261–75.
36. Lehtinen MK, Walsh CA. Neurogenesis at the brain-cerebrospinal fluid interface. *Annu Rev Cell Dev Biol.* 2011;27:653.
37. Pan S, Yang PH, DeFreitas D, Ramagiri S, Bayguinov PO, Hacker CD, et al. Gold nanoparticle-enhanced X-ray microtomography of the rodent reveals region-specific cerebrospinal fluid circulation in the brain. *Nat Commun.* 2023;14:1–16.
38. Derk J, Jones HE, Como C, Pawlikowski B, Siegenthaler JA. Living on the edge of the CNS: meninges cell diversity in health and disease. *Front Cell Neurosci.* 2021;15: 703944.
39. Vivatbutsirir P, Ichinose S, Hytönen M, Sainio K, Eto K, Iseki S. Impaired meningeal development in association with apical expansion of calvarial bone osteogenesis in the Foxc1 mutant. *J Anat.* 2008;212:603.
40. Siegenthaler JA, Ashique AM, Zarbalis K, Patterson KP, Hecht JH, Kane MA, et al. Retinoic acid from the meninges regulates cortical neuron generation. *Cell.* 2009;139:597–609.
41. Dasgupta K, Jeong J. Developmental biology of the meninges. *Genesis.* 2019;57: e23288.
42. Derk J, Como CN, Jones HE, Joyce LR, Kim S, Spencer BL, et al. Formation and function of the meningeal arachnoid barrier around the developing mouse brain. *Dev Cell.* 2023;58: e01675.
43. Shenoy SS, Lui F. Neuroanatomy, Ventricular System. *StatPearls.* 2021. <https://www.ncbi.nlm.nih.gov/books/NBK532932/>. Accessed 13 Jul 2022.
44. Maillot C, Koritke JG, Laude M. La vascularisation de la toile choroïdienne du quatrième ventricule chez le chat (*felis domestica*). *Archives d'Anatomie, d'Histologie et d'Embryologie.* 1978;61:3–42.
45. Wolfram-Gabel R, Maillot C, Koritke JG, Laude M. [Vascularization of the tela choroidea of the 3rd ventricle in man]. *Arch Anat Histol Embryol.* 1984;67:3–42.
46. de Melo Mussi AC, Matushita H, Andrade FG, Rhoton AL. Surgical approaches to IV ventricle—anatomical study. *Childs Nerv Syst.* 2015;31:1807–14.
47. Tsutsumi S, Ishii H, Ono H, Yasumoto Y. The third ventricle roof: an anatomical study using constructive interference in steady-state magnetic resonance imaging. *Surg Radiol Anat.* 2018;40:123–8.
48. Strong LH. The vascular and ependymal development of the early stages of the tela choroidea of the lateral ventricle of the mammal. *J Morphol.* 1964;114:59–82.
49. Leucio A de, Dossani RH. Cavum Veli Interpositi. *Radiopaedia.org.* 2021. <https://www.ncbi.nlm.nih.gov/books/NBK559000/>. Accessed 13 July 2022.
50. Zhang XA, Qi S, Fan J, Huang G, Peng J, Xu J. The distribution of arachnoid membrane within the velum interpositum. *Acta Neurochir (Wien).* 2012;154:1711–5.
51. Hashimoto PH. Tracer in cisternal cerebrospinal fluid is soon detected in choroid plexus capillaries. *Brain Res.* 1988;440:149–52.
52. Maurizi CP. Recirculation of cerebrospinal fluid through the tela choroidea is why high levels of melatonin can be found in the lateral ventricles. *Med Hypotheses.* 1991;35:154–8.
53. Maurizi CP. The pathophysiology of enlarged ventricles in normal pressure communicating hydrocephalus and schizophrenia: a possible therapeutic role for melatonin. *Med Hypotheses.* 1987;23:61–6.
54. Fame RM, Xu H, Pragma A, Lehtinen M. Age-appropriate potassium clearance from perinatal cerebrospinal fluid depends on choroid plexus NKCC1. *Fluids Barriers CNS.* 2023;20:45.
55. Xu H, Fame RM, Sadegh C, Sutin J, Naranjo C, Syau D, et al. Choroid plexus NKCC1 mediates cerebrospinal fluid clearance during mouse early post-natal development. *Nat Commun.* 2021;12:1–16.
56. Kida S, Pantazis A, Weller RO. CSF drains directly from the subarachnoid space into nasal lymphatics in the rat. Anatomy, histology and immunological significance. *Neuropathol Appl Neurobiol.* 1993;19:480.
57. Aspelund A, Antila S, Proulx ST, Karlsen TV, Karaman S, Detmar M, et al. A dural lymphatic vascular system that drains brain interstitial fluid and macromolecules. *J Exp Med.* 2015;212:991.
58. Mezey É, Szalayova I, Hogden CT, Brady A, Dósa Á, Sótonyi P, et al. An immunohistochemical study of lymphatic elements in the human brain. *Proc Natl Acad Sci U S A.* 2021;118: e2002574118.
59. Zhang ET, Richards HK, Kida S, Weller RO. Directional and compartmentalised drainage of interstitial fluid and cerebrospinal fluid from the rat brain. *Acta Neuropathol.* 1992;83:233–9.
60. Kida S, Weller RO, Zhang E-T, Phillips MJ, Iannotti F. Anatomical pathways for lymphatic drainage of the brain and their pathological significance. *Neuropathol Appl Neurobiol.* 1995;21:181–4.
61. Weller RO, Kida S, Zhang E-T. Pathways of fluid drainage from the brain - morphological aspects and immunological significance in rat and man. *Brain Pathol.* 1992;2(4):277–84.
62. Papaiconomou C, Zakharov A, Azizi N, Djenic J, Johnston M. Reassessment of the pathways responsible for cerebrospinal fluid absorption in the neonate. *Child's Nerv Syst.* 2004;20:29–36.
63. Wang YJ, Sun YR, Pei YH, Ma HW, Mu YK, Qin LH, et al. The lymphatic drainage systems in the brain: a novel target for ischemic stroke? *Neural Regen Res.* 2023;18(3):485–91.
64. Johnston M, Zakharov A, Papaiconomou C, Salmasi G, Armstrong D. Evidence of connections between cerebrospinal fluid and nasal lymphatic vessels in humans, non-human primates and other mammalian species. *Cerebrospinal Fluid Res.* 2004;1:2.
65. Zakharov A, Papaiconomou C, Djenic J, Midha R, Johnston M. Lymphatic cerebrospinal fluid absorption pathways in neonatal sheep revealed by subarachnoid injection of Microfil. *Neuropathol Appl Neurobiol.* 2003;29:563–73.
66. Zakharov A, Papaiconomou C, Johnston M. Lymphatic vessels gain access to cerebrospinal fluid through unique association with olfactory nerves. *Lymphat Res Biol.* 2004;2:139.
67. Mortensen OA, Sullivan WE. The cerebrospinal fluid and the cervical lymph nodes. *Anat Rec.* 1933;56:359.
68. Brinker T, Lüdemann W, Von Rautenfeld Berens D, Samii M. Dynamic properties of lymphatic pathways for the absorption of cerebrospinal fluid. *Acta Neuropathol.* 1997;94:493.
69. Kiwic G, Slusarczyk K, Slusarczyk R. The central nervous system and the lymphatic system. Lymphatic drainage of the cerebrospinal fluid. *Neurol Neurochir Pol.* 1998;32(3):633–41.
70. Krisch B, Leonhardt H, Oksche A. The meningeal compartments of the median eminence and the cortex - a comparative analysis in the rat. *Cell Tissue Res.* 1983;228:597–640.
71. Johanson CE, Stopa EG, McMillan PN. The blood-cerebrospinal fluid barrier: structure and functional significance. *Methods Mol Biol.* 2011;686:101–31.
72. Tumani H, Huss A, Bachhuber F. The cerebrospinal fluid and barriers – anatomic and physiologic considerations. *Handb Clin Neurol.* 2017;146:21–32.
73. Pietilä R, Del Gaudio F, He L, Vázquez-Liébanas E, Vanlandewijck M, Muhl L, et al. Molecular anatomy of adult mouse leptomeninges. *Neuron.* 2023;111:3745.
74. Nabeshima S, Reese TS, Landis DMD, Brightman MW. Junctions in the meninges and marginal glia. *J Comp Neurol.* 1975;164:127.
75. Saunders NR, Ek CJ, Habgood MD, Dziegielewska KM. Barriers in the brain: a renaissance? *Trends Neurosci.* 2008;31:279.

Publisher's Note

Springer Nature remains neutral with regard to jurisdictional claims in published maps and institutional affiliations.

Ready to submit your research? Choose BMC and benefit from:

- fast, convenient online submission
- thorough peer review by experienced researchers in your field
- rapid publication on acceptance
- support for research data, including large and complex data types
- gold Open Access which fosters wider collaboration and increased citations
- maximum visibility for your research: over 100M website views per year

At BMC, research is always in progress.

Learn more biomedcentral.com/submissions

